

Optimal low-order fully integrated solid-shell elements

K. Rah · W. Van Paepegem · A. M. Habraken ·
J. Degrieck · R. J. Alves de Sousa · R. A. F. Valente

Received: 12 December 2011 / Accepted: 5 May 2012 / Published online: 26 June 2012
© Springer-Verlag 2012

Abstract This paper presents three optimal low-order fully integrated geometrically nonlinear solid-shell elements based on the enhanced assumed strain (EAS) method and the assumed natural strain method for different types of structural analyses, e.g. analysis of thin homogeneous isotropic and multilayer anisotropic composite shell-like structures and the analysis of (near) incompressible materials. The proposed solid-shell elements possess eight nodes with only displacement degrees of freedom and a few internal EAS parameters. Due to the 3D geometric description of the proposed elements, 3D constitutive laws can directly be employed in these formulations. The present formulations are based on the well-known Fraeijns de Veubeke–Hu–Washizu multifield variational principle. In terms of accuracy as well as efficiency point of view, the choice of the optimal EAS parameters plays a very critical role in the EAS method, therefore a systematic numerical study has been carried out to find out the optimal EAS parameters to alleviate different locking phenomena for the proposed solid-shell formulations. To assess the accuracy of the proposed solid-shell elements, a variety of popular numerical benchmark examples related to element convergence, mesh distortions, element aspect ratios and different locking phenomena are investigated and

the results are compared with the well-known solid-shell formulations available in the literature. The results of our numerical assessment show that the proposed solid-shell formulations provide very accurate results, without showing any numerical problems, for a variety of geometrically linear and nonlinear structural problems.

Keywords Solid-shell element · Enhanced assumed strain method · Assumed natural strain method · Shell-like structures · Multifield variational principle · Locking

1 Introduction

A significant amount of research work has been published over the last few years on the development of accurate and efficient low-order solid-shell formulations, e.g. see [1–12]. This is due to the numerous advantages solid-shell elements offer when compared to their conventional shell element counterparts. Most of the well-known fully integrated low-order solid-shell formulations, e.g. see [5, 6, 8, 9, 13–17], employ the enhanced assumed strain (EAS) method proposed by Simo and Rifai [18] to alleviate thickness and volumetric locking, to improve the element convergence and to increase the mesh distortion insensitivity. The EAS method has proved to be very effective when it comes to alleviate these element pathologies. In earlier days, the main disadvantage of the EAS method was its computational inefficiency, owing to the large number of strain enhancing parameters introduced in the formulation. For example, 30 EAS parameters are employed in the EAS based method in [19, 20]. In order to alleviate the locking problems in an EAS based solid-shell element, the selection of the optimal EAS parameters is a very crucial issue. An increased number of EAS parameters is computationally demanding, therefore these parameters

K. Rah (✉) · W. V. Paepegem · J. Degrieck
Department of Materials Science and Engineering, Ghent
University, Sint-Pietersnieuwstraat 41, 9000 Gent, Belgium
e-mail: kami861@hotmail.com

A. M. Habraken
Mécanique des Solides, des Fluides et des Structures,
Université de Liège, chemin des Chevreuils 1, bât B52/3,
4000 Liège, Belgium

R. J. A. de Sousa · R. A. F. Valente
Department of Mechanical Engineering, University of Aveiro,
Aveiro, Portugal

should be selected carefully. A trade-off between the accuracy and the computational efficiency is required to exploit the full benefits of the EAS method.

The optimal choice of the EAS parameters can be made based on the type of analysis for which the solid-shell elements will be used. For example, considering the fact that incompressibility is not an issue in the analyses of multilayer composites due to the brittle nature of composite materials, a solid-shell element that is formulated to analyze multilayer composites must not contain the additional EAS parameters to resolve the volumetric locking phenomenon, thereby saving the computational time. However, in order to make an optimal choice of these parameters regarding different types of analyses, the EAS parameters related to the different solid-shell element issues, like locking problems, element convergence and mesh distortion need to be clearly identified.

This work provides a number of low-order fully integrated solid-shell elements based on the effective combination of the EAS and assumed natural strain (ANS) methods. Optimal number of EAS parameters has been employed in the proposed solid-shell formulations to alleviate different types of numerical pathologies, thereby leading to enhanced computational efficiency. In order to determine the optimal EAS parameters, a systematic numerical investigation has been carried out to choose the optimal number of these parameters regarding the previously mentioned element issues in the fully integrated low-order solid-shell elements. Similar to other well-known solid-shell formulations in the literature [5,6,8,9,16], we employ the ANS method in the present solid-shell formulations to alleviate the transverse shear and trapezoidal locking issues.

The first solid-shell element, the so-called EAS3ANS, employs only three EAS parameters passing both the membrane and the out-of-plane bending patch tests and showing excellent results in extremely high element length-to-thickness aspect ratios, making it very suitable for the analysis of thin multilayer composites. The second solid-shell element, the so-called EAS7ANS1 element, is the extension of the EAS3ANS element, where four additional EAS parameters have been introduced, leading to in total seven EAS parameters, in order to alleviate the volumetric locking completely. The EAS7ANS1 element is suitable for the analysis of near incompressible materials, like hyperelastic and elasto-plastic analyses. The third solid-shell element, the so-called EAS7ANS2 element, is also the extension of the EAS3ANS element, where four additional EAS parameters have been introduced, giving in total seven EAS parameters, in order to decrease the element sensitivity for high mesh distortions. The EAS7ANS2 element provides accurate results for coarse highly distorted meshes, thereby making it attractive for the engineering industrial sector, where due to the time limitations relatively coarse and irregular meshes are generally used to save the time-costly pre-processing effort.

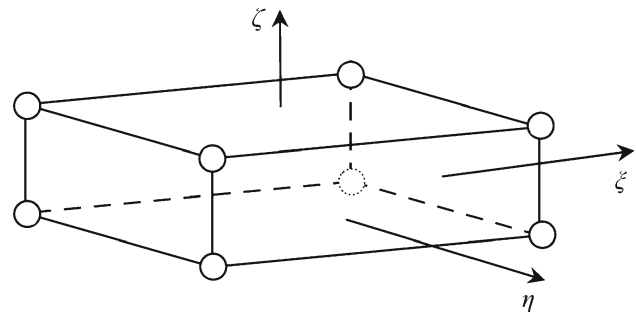


Fig. 1 Solid-shell element in isoparametric space

The outline of the paper is as follows. In sect. 2 the kinematic assumptions of the solid-shell element and the nonlinear issues will be discussed briefly. In sect. 3 the nonlinear EAS formulation will be explained. Section 4 provides a brief description of the ANS method. In sects. 5 and 6 the state-of-the-art and proposed EAS parameters for the present solid-shell elements will be discussed, respectively. In sect. 7 the numerical performance of the proposed solid-shell elements will be assessed and compared with a variety of popular shell/solid-shell elements employing numerical benchmark examples from the literature. Finally, conclusions will be formulated in sect. 8.

2 Kinematic assumptions

For the present solid-shell element, the kinematic assumption of the shear deformable shells is applied. According to this assumption the normal to the element mid-surface remains straight but not necessarily normal during the deformation. This assumption is fulfilled by a linear approximation of the in-plane displacements over the shell thickness [8]. Figure 1 shows the solid-shell geometry where $\mathbf{s} = (\xi, \eta, \zeta)$ are the natural coordinates $[-1, +1]$.

The updated Lagrange approach has been employed here to take the geometrical nonlinearity into account for a solid-shell formulation. Three configurations can be figured out in the updated Lagrange approach, namely the parametric (convective) configuration, the reference (material) configuration and the current (spatial) configuration. The reference configuration here refers to a converged state (n) in the last increment and the current configuration denotes the unknown state ($n+1$) corresponding to the next increment. The position vector (\mathbf{X}) of any point in the reference and current configurations reads as follows:

$${}^n\mathbf{X}(\xi, \eta, \zeta) = \frac{1}{2}(1 + \zeta) {}^n\mathbf{X}_T + \frac{1}{2}(1 - \zeta) {}^n\mathbf{X}_B \quad (1)$$

$${}^{n+1}\mathbf{X}(\xi, \eta, \zeta) = \frac{1}{2}(1 + \zeta) {}^{n+1}\mathbf{X}_T + \frac{1}{2}(1 - \zeta) {}^{n+1}\mathbf{X}_B \quad (2)$$

The reference configuration is related to the current configuration by the displacement field \mathbf{u} as follows:

$${}^{n+1}\mathbf{X}(\mathbf{s}) = {}^n\mathbf{X}(\mathbf{s}) + {}^{n+1}\mathbf{u}(\mathbf{s}) \quad (3)$$

The covariant basis vectors in the current and reference configurations are related to the position vector \mathbf{X} as follows:

$${}^{n+1}\mathbf{G}_i = \frac{\partial {}^{n+1}\mathbf{X}}{\partial \mathbf{s}_i}; \quad {}^n\mathbf{G}_i = \frac{\partial {}^n\mathbf{X}}{\partial \mathbf{s}_i} \quad (4)$$

The incremental deformation gradient (\mathbf{F}) and the displacement-based Green–Lagrange strain tensor $\boldsymbol{\varepsilon}^c$ between the reference and current configurations can then be written as follows:

$${}^{n+1}{}_n\mathbf{F} = \frac{\partial {}^{n+1}\mathbf{X}}{\partial {}^n\mathbf{X}} \quad (5)$$

$${}^{n+1}{}_n\boldsymbol{\varepsilon}^c = \frac{1}{2} \left({}^{n+1}{}_n\mathbf{F}^T {}^{n+1}{}_n\mathbf{F} - \mathbf{I}_2 \right) \quad (6)$$

$${}^{n+1}{}_n\varepsilon_{ab}^c = \frac{1}{2} \left(\underbrace{{}^n\mathbf{G}_a \cdot \frac{\partial {}^{n+1}\mathbf{u}}{\partial {}^n\mathbf{s}_b} + {}^n\mathbf{G}_b \cdot \frac{\partial {}^{n+1}\mathbf{u}}{\partial {}^n\mathbf{s}_a}}_{\text{linearpart}} + \underbrace{\frac{\partial {}^{n+1}\mathbf{u}}{\partial {}^n\mathbf{s}_a} \cdot \frac{\partial {}^{n+1}\mathbf{u}}{\partial {}^n\mathbf{s}_b}}_{\text{non-linearpart}} \right); \quad (7)$$

$a, b = 1, 2, 3$

where \mathbf{I}_2 is the second-order identity tensor. The second Piola–Kirchhoff stress tensor $\boldsymbol{\sigma}$ is considered as the work conjugate of the Green–Lagrange strain tensor $\boldsymbol{\varepsilon}^c$:

$$\boldsymbol{\sigma} = \sigma^{ab} {}^n\mathbf{G}_a \otimes {}^n\mathbf{G}_b \quad (8)$$

3 Nonlinear EAS formulation

The EAS method was originally proposed by Simo and Rifai [18] and is based on the three-field Veubeke–Hu–Washizu variational principle [21–23]:

$$\prod^{\text{FW}}(\mathbf{u}, \boldsymbol{\varepsilon}, \boldsymbol{\sigma}) = \int_{\Omega} W(\boldsymbol{\varepsilon}) + \boldsymbol{\sigma} : \left[\frac{1}{2}(\mathbf{F}^T\mathbf{F} - \mathbf{I}_2) - \boldsymbol{\varepsilon} \right] d\Omega - \prod^{\text{ext}} \quad (9)$$

$$\prod^{\text{ext}} = \int_{\Omega} \mathbf{p}^* \cdot \mathbf{u} d\Omega + \int_{\partial\Omega_{\sigma}} \mathbf{t}^* \cdot \mathbf{u} d\partial\Omega \quad (10)$$

where the displacement field \mathbf{u} , the Green–Lagrange strain tensor $\boldsymbol{\varepsilon}$ and the second Piola–Kirchhoff stress tensor $\boldsymbol{\sigma}$ are the independent variables, and displacement boundary conditions are satisfied a priori. The variables with superscript “c” are derived from the displacement field. Here, \mathbf{p}^* and \mathbf{t}^* are the prescribed body forces and traction vectors, respectively.

For geometrical nonlinear analyses, there are two ways to introduce the EAS method. In the first approach the deformation gradient \mathbf{F} is enhanced [9, 24], while in the second approach the Green–Lagrange strain tensor $\boldsymbol{\varepsilon}$ is enhanced [2, 20]. Both methods lead to the same numerical results when the same EAS parameters are used, however the second is computationally simpler and more efficient. The advantages of the second approach are discussed by Andelfinger and Ramm [19] for linear cases and by Bischoff and Ramm [2] for nonlinear cases. Therefore, the enhancement of the Green–Lagrange strain tensor $\boldsymbol{\varepsilon}$ will be adopted in this section.

The core idea behind the EAS method is the enhancement of the compatible strain field $\boldsymbol{\varepsilon}^c$ with a so-called enhancing strain field $\boldsymbol{\varepsilon}^{\alpha}$, and assuming the orthogonality condition between the stress field $\boldsymbol{\sigma}$ and the enhancing strain field $\boldsymbol{\varepsilon}^{\alpha}$, leads to the following form of the functional in (9):

$$\prod(\mathbf{u}, \boldsymbol{\varepsilon}^{\alpha}) = \int_{\Omega} W(\boldsymbol{\varepsilon}^c(\mathbf{u}) + \boldsymbol{\varepsilon}^{\alpha}) d\Omega - \prod^{\text{ext}} \quad (11)$$

$$\int_{\Omega} \boldsymbol{\sigma} : \boldsymbol{\varepsilon}^{\alpha} d\Omega = 0 \quad (12)$$

The variation of the modified functional in (11) can be obtained from the Gateaux or directional derivative, leading to the total variation [5]:

$$\delta \prod(\mathbf{u}, \boldsymbol{\varepsilon}^{\alpha}) = \delta \prod^{\text{int}} - \delta \prod^{\text{ext}} \quad (13)$$

$$\delta \prod^{\text{int}} = \int_{\Omega} (\delta \boldsymbol{\varepsilon} + \delta \boldsymbol{\varepsilon}^{\alpha}) : \frac{\delta W(\boldsymbol{\varepsilon} + \boldsymbol{\varepsilon}^{\alpha})}{\delta(\boldsymbol{\varepsilon} + \boldsymbol{\varepsilon}^{\alpha})} d\Omega \quad (14)$$

$$\delta \prod^{\text{ext}} = \int_{\Omega} \mathbf{p}^* \cdot \delta \mathbf{u} d\Omega + \int_{\partial\Omega_{\sigma}} \mathbf{t}^* \cdot \delta \mathbf{u} d\partial\Omega \quad (15)$$

The weak form can now be expanded employing a truncated Taylor series at the n th state $(\mathbf{u}|_n, \boldsymbol{\varepsilon}^{\alpha}|_n)$ as follows:

$$\delta \prod(\mathbf{u}|_{n+1}, \boldsymbol{\varepsilon}^{\alpha}|_{n+1}) \approx \delta \prod(\mathbf{u}|_n, \boldsymbol{\varepsilon}^{\alpha}|_n) + \mathcal{D}[\delta \prod](\mathbf{u}|_n, \boldsymbol{\varepsilon}^{\alpha}|_n) \cdot \left({}^{n+1}_n\mathbf{u}, {}^{n+1}_n\boldsymbol{\varepsilon}^{\alpha} \right) \quad (16)$$

The displacement field \mathbf{u} , its variation $\delta \mathbf{u}$ and its increment ${}^{n+1}_n\mathbf{u}$ is interpolated in each element domain as follows:

$$\mathbf{u} \approx \mathbf{u}^h = \mathbf{N}(\mathbf{s}) \mathbf{d} \quad (17)$$

$$\delta \mathbf{u} \approx \delta \mathbf{u}^h = \mathbf{N}(\mathbf{s}) \delta \mathbf{d} \quad (18)$$

$${}^{n+1}_n\mathbf{u} \approx {}^{n+1}_n\mathbf{u}^h = \mathbf{N}(\mathbf{s}) {}^{n+1}_n\mathbf{d} \quad (19)$$

where the superscript “h” refers to the approximated values and matrix \mathbf{N} contains the usual isoparametric compatible

shape functions for a 3D element, relating the continuum displacement field \mathbf{u} and the corresponding vector of 24 translational degrees-of-freedom \mathbf{d} of the eight-node brick element.

The enhanced Green–Lagrange strain tensor $\boldsymbol{\varepsilon}$ (also its variation $\delta\boldsymbol{\varepsilon}$) can be interpolated all over the element domain using the vectors \mathbf{d} and the enhancing strain parameter $\boldsymbol{\alpha}$ as follows:

$$\boldsymbol{\varepsilon} = \boldsymbol{\varepsilon}^c + \boldsymbol{\varepsilon}^\alpha = [\mathbf{B} \ \mathbf{M}] \begin{bmatrix} \mathbf{d} \\ \boldsymbol{\alpha} \end{bmatrix} \quad (20)$$

$$\boldsymbol{\varepsilon} = [\varepsilon_{xx} \ \varepsilon_{yy} \ \varepsilon_{zz} \ \gamma_{xy} \ \gamma_{xz} \ \gamma_{yz}]^T \quad (21)$$

where \mathbf{B} is the well-known strain-displacement matrix and \mathbf{M} contains the trial functions corresponding to the enhancing strain field $\boldsymbol{\varepsilon}^\alpha$. The matrix \mathbf{M} is generally defined in the natural coordinates of the element, and the following transformation is needed to transform it to the physical Cartesian space, as proposed by Simo and Rifai [18]:

$$\mathbf{M} = \frac{|\mathbf{J}_0|}{|\mathbf{J}|} \mathbf{T}_0 \tilde{\mathbf{M}} \quad (22)$$

where the matrices \mathbf{M} and $\tilde{\mathbf{M}}$ contain the trial functions of the enhancing strain field $\boldsymbol{\varepsilon}^{\text{enh}}$ in natural and physical Cartesian coordinate systems respectively, and $|\mathbf{J}_0|$ and $|\mathbf{J}|$ are the determinants of the Jacobian matrices at the element center and at any arbitrary point in the element domain respectively. The determinants of the Jacobians are needed to enforce the orthogonality condition between the stress field $\boldsymbol{\sigma}$ and the enhancing strain field $\boldsymbol{\varepsilon}^\alpha$ for the constant stress and strain states, i.e. the element patch test. The transformation matrix \mathbf{T}_0 reads as follows:

$$\mathbf{T}_0 = \begin{bmatrix} J_{11}^{-1} J_{11}^{-1} & J_{12}^{-1} J_{12}^{-1} & J_{13}^{-1} J_{13}^{-1} & J_{11}^{-1} J_{12}^{-1} \\ J_{21}^{-1} J_{21}^{-1} & J_{22}^{-1} J_{22}^{-1} & J_{23}^{-1} J_{23}^{-1} & J_{21}^{-1} J_{22}^{-1} \\ J_{31}^{-1} J_{31}^{-1} & J_{32}^{-1} J_{32}^{-1} & J_{33}^{-1} J_{33}^{-1} & J_{31}^{-1} J_{32}^{-1} \\ 2J_{11}^{-1} J_{21}^{-1} & 2J_{12}^{-1} J_{22}^{-1} & 2J_{13}^{-1} J_{23}^{-1} & J_{11}^{-1} J_{22}^{-1} + J_{12}^{-1} J_{21}^{-1} \\ 2J_{21}^{-1} J_{31}^{-1} & 2J_{22}^{-1} J_{32}^{-1} & 2J_{23}^{-1} J_{33}^{-1} & J_{21}^{-1} J_{32}^{-1} + J_{22}^{-1} J_{31}^{-1} \\ 2J_{11}^{-1} J_{31}^{-1} & 2J_{12}^{-1} J_{32}^{-1} & 2J_{13}^{-1} J_{33}^{-1} & J_{11}^{-1} J_{32}^{-1} + J_{12}^{-1} J_{31}^{-1} \\ J_{12}^{-1} J_{13}^{-1} & J_{11}^{-1} J_{13}^{-1} & J_{21}^{-1} J_{23}^{-1} & J_{21}^{-1} J_{23}^{-1} \\ J_{22}^{-1} J_{23}^{-1} & J_{21}^{-1} J_{23}^{-1} & J_{31}^{-1} J_{33}^{-1} & J_{31}^{-1} J_{33}^{-1} \\ J_{12}^{-1} J_{23}^{-1} + J_{22}^{-1} J_{13}^{-1} & J_{11}^{-1} J_{23}^{-1} + J_{21}^{-1} J_{13}^{-1} & J_{21}^{-1} J_{33}^{-1} + J_{31}^{-1} J_{23}^{-1} & J_{21}^{-1} J_{33}^{-1} + J_{31}^{-1} J_{23}^{-1} \\ J_{22}^{-1} J_{33}^{-1} + J_{32}^{-1} J_{23}^{-1} & J_{21}^{-1} J_{33}^{-1} + J_{31}^{-1} J_{23}^{-1} & J_{31}^{-1} J_{33}^{-1} + J_{33}^{-1} J_{31}^{-1} & J_{31}^{-1} J_{33}^{-1} + J_{33}^{-1} J_{31}^{-1} \end{bmatrix} \quad (23)$$

where J_{ik}^{-1} are the components of the inverse of the Jacobian matrix \mathbf{J}^{-1} evaluated at the element center.

$$\mathbf{J}^{-1} = \begin{bmatrix} J_{11}^{-1} & J_{12}^{-1} & J_{13}^{-1} \\ J_{21}^{-1} & J_{22}^{-1} & J_{23}^{-1} \\ J_{31}^{-1} & J_{32}^{-1} & J_{33}^{-1} \end{bmatrix} = \begin{bmatrix} \frac{\partial \xi}{\partial x} & \frac{\partial \eta}{\partial x} & \frac{\partial \zeta}{\partial x} \\ \frac{\partial \xi}{\partial y} & \frac{\partial \eta}{\partial y} & \frac{\partial \zeta}{\partial y} \\ \frac{\partial \xi}{\partial z} & \frac{\partial \eta}{\partial z} & \frac{\partial \zeta}{\partial z} \end{bmatrix}_{(\xi, \eta, \zeta) = (0, 0, 0)} \quad (24)$$

Now considering the interpolation assumptions of Eqs. (17)–(20), the second term on the right-hand side of the linearized weak form in (16) can be rewritten, dropping the iteration indices, as follows [2, 5, 20]:

$$\mathcal{D} \left[\delta \prod \right] (\mathbf{d}, \boldsymbol{\alpha}) \cdot ({}^{n+1}_n \mathbf{d}, {}^{n+1}_n \boldsymbol{\alpha}) = \frac{\delta(\delta \prod^{\text{int}} - \delta \prod^{\text{ext}})}{\delta(\mathbf{d}, \boldsymbol{\alpha})} \cdot ({}^{n+1}_n \mathbf{d}, {}^{n+1}_n \boldsymbol{\alpha}) \quad (25)$$

where the variations $\delta \prod^{\text{int}}$ and $\delta \prod^{\text{ext}}$ are given as:

$$\delta \prod^{\text{int}} (\mathbf{d}, \boldsymbol{\alpha}) = \delta \mathbf{d}^T \int_{\Omega} \mathbf{B}^T \boldsymbol{\sigma} d\Omega + \delta \boldsymbol{\alpha}^T \int_{\Omega} \mathbf{M}^T \boldsymbol{\sigma} d\Omega \quad (26)$$

$$\delta \prod^{\text{ext}} (\mathbf{d}) = \delta \mathbf{d}^T \int_{\Omega} \mathbf{N}^T \mathbf{p}^* d\Omega + \delta \mathbf{d}^T \int_{\partial\Omega_\sigma} \mathbf{N}^T \mathbf{t}^* d\partial\Omega \quad (27)$$

Focusing on the variation of the internal part of the whole potential $\delta \prod^{\text{int}}$, it can be rewritten as follows [25]:

$$\begin{aligned} \mathcal{D} \left[\delta \prod^{\text{int}} \right] \cdot ({}^{n+1}_n \mathbf{d}, {}^{n+1}_n \boldsymbol{\alpha}) &= \frac{\delta(\delta \prod^{\text{int}})}{\delta \mathbf{d}} \cdot {}^{n+1}_n \mathbf{d} \\ &+ \frac{\delta(\delta \prod^{\text{int}})}{\delta \boldsymbol{\alpha}} \cdot {}^{n+1}_n \boldsymbol{\alpha} = \delta \mathbf{d}^T \left[(\mathbf{K}_{\text{lg}}^{uu} + \mathbf{K}_{\text{nlg}}^{uu}) {}^{n+1}_n \mathbf{d} + \mathbf{K}^{u\alpha} {}^{n+1}_n \boldsymbol{\alpha} \right] \\ &+ \delta \boldsymbol{\alpha}^T \left[\mathbf{K}^{\alpha u} {}^{n+1}_n \mathbf{d} + \mathbf{K}^{\alpha\alpha} {}^{n+1}_n \boldsymbol{\alpha} \right], \quad (\forall \delta \mathbf{d}, \delta \boldsymbol{\alpha}) \end{aligned} \quad (28)$$

where $\mathbf{K}_{\text{lg}}^{uu}$ is the standard displacement-based stiffness matrix, and $\mathbf{K}^{u\alpha}$, $\mathbf{K}^{\alpha u}$, and $\mathbf{K}^{\alpha\alpha}$ are the well-known EAS-based stiffness matrices [18] and matrix $\mathbf{K}_{\text{nlg}}^{uu}$ is the initial stress stiffness matrix, given as follows:

$$\mathbf{K}_{\text{lg}}^{uu} = \int_{\Omega} \mathbf{B}^T \mathbf{C} \mathbf{B} d\Omega \quad (29)$$

$$\mathbf{K}^{u\alpha} = \int_{\Omega} \mathbf{B}^T \mathbf{C} \mathbf{M} d\Omega \quad (30)$$

$$\mathbf{K}^{\alpha u} = \int_{\Omega} \mathbf{M}^T \mathbf{C} \mathbf{B} d\Omega \quad (31)$$

$$\mathbf{K}^{\alpha\alpha} = \int_{\Omega} \mathbf{M}^T \mathbf{C} \mathbf{M} d\Omega \quad (32)$$

$$\mathbf{K}_{\text{nlg}}^{uu} = \int_{\Omega} \mathbf{B}_{\text{nlg}}^T \boldsymbol{\sigma}_g \mathbf{B}_{\text{nlg}} d\Omega \quad (33)$$

where \mathbf{C} is the material elasticity matrix and \mathbf{B}_{nlg} is the strain-displacement matrix described in the physical local frame \mathbf{r} as follows:

$$\mathbf{B}_{\text{nlg}} = \begin{bmatrix} N_{r,1} & 0 & 0 \\ N_{r,2} & 0 & 0 \\ N_{r,3} & 0 & 0 \\ 0 & N_{r,1} & 0 \\ 0 & N_{r,2} & 0 \\ 0 & N_{r,3} & 0 \\ 0 & 0 & N_{r,1} \\ 0 & 0 & N_{r,2} \\ 0 & 0 & N_{r,3} \end{bmatrix} \quad \text{with } N_{r,j} = \frac{\partial N}{\partial s_i} \frac{\partial s_i}{\partial r^j} \quad (34)$$

node k

for $k = 1, 2, \dots, 8$. The 9×9 array σ_9 is composed of the sub-blocks of the stress tensor written in the following array form and evaluated at each Gauss point:

$$\sigma_9 = \begin{bmatrix} \sigma_3 & 0 & 0 \\ 0 & \sigma_3 & 0 \\ 0 & 0 & \sigma_3 \end{bmatrix} \quad (35)$$

Finally, the adopted additive approach to enhance the Green–Lagrange strains (20) leads to a straightforward algorithmic extension of the linear EAS formulation by Simo and Rifai [18], without any involvement of coupling nonlinear geometric stiffness matrices associated with the enhanced variables [2], and providing the following discrete linearized final system of equations [5, 20]:

$$\begin{bmatrix} \mathbf{K}_{\text{lg}}^{uu} + \mathbf{K}_{\text{nlg}}^{uu} & \mathbf{K}^{u\alpha} \\ \mathbf{K}^{\alpha u} & \mathbf{K}^{\alpha\alpha} \end{bmatrix} \begin{bmatrix} {}^{n+1}_n \mathbf{d} \\ {}^{n+1}_n \boldsymbol{\alpha} \end{bmatrix} = \begin{bmatrix} \mathbf{f}_u^{\text{ext}} \\ 0 \end{bmatrix} - \begin{bmatrix} \mathbf{f}_u^{\text{int}} \\ \mathbf{f}_\alpha^{\text{int}} \end{bmatrix} \quad (36)$$

where the increment indices are omitted for the notations' convenience. The external and internal force vectors are calculated as follows:

$$\mathbf{f}_u^{\text{ext}} = \int_{\Omega} \mathbf{N}^T \mathbf{p}^* d\Omega + \int_{\partial\Omega_\sigma} \mathbf{N}^T \mathbf{t}^* d\partial\Omega \quad (37)$$

$$\mathbf{f}_u^{\text{int}} = \int_{\Omega} \mathbf{B}^T \boldsymbol{\sigma} d\Omega \quad (38)$$

$$\mathbf{f}_\alpha^{\text{int}} = \int_{\Omega} \mathbf{M}^T \boldsymbol{\sigma} d\Omega \quad (39)$$

Now the static condensation of the enhancing strain parameters ${}^{n+1}_n \boldsymbol{\alpha}$ at the element level from the system of equations in (36) leads to the following element system of equations:

$$\mathbf{K}^{u+\alpha} {}^{n+1}_n \mathbf{d} = \mathbf{f}^{u+\alpha} \quad (40)$$

$$\mathbf{K}^{u+\alpha} = \mathbf{K}_{\text{lg}}^{uu} + \mathbf{K}_{\text{nlg}}^{uu} - \mathbf{K}^{u\alpha} (\mathbf{K}^{\alpha\alpha})^{-1} \mathbf{K}^{\alpha u} \quad (41)$$

$$\mathbf{f}^{u+\alpha} = \mathbf{f}_u^{\text{ext}} - \mathbf{f}_u^{\text{int}} + \mathbf{K}^{u\alpha} (\mathbf{K}^{\alpha\alpha})^{-1} \mathbf{f}_\alpha^{\text{int}} \quad (42)$$

As only the displacement DOF are left in the final system of equations in (40), the overall solution procedure of the

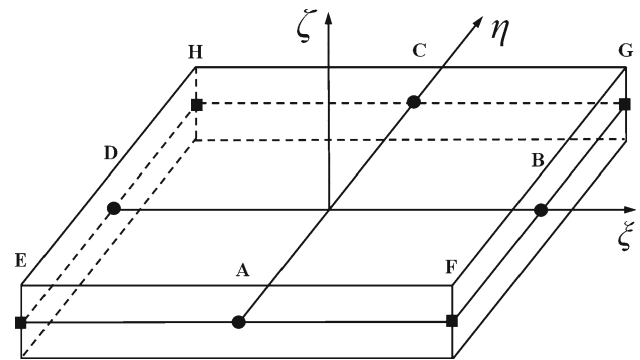


Fig. 2 Sampling points shown on solid-shell element for ANS interpolation

EAS formulation does not differ from a standard displacement-based FE formulation. The incremental displacement ${}^{n+1}_n \mathbf{d}$ can be computed by using (40) and the displacement \mathbf{d} is updated accordingly. The incremental displacement ${}^{n+1}_n \mathbf{d}$ can be used to solve the ${}^{n+1}_n \boldsymbol{\alpha}$, employing the second equation of the discrete linearized final system of equations in (36), which in turn is used to update the EAS parameters $\boldsymbol{\alpha}$. For further detailed description of the formulation, we refer the reader to [4].

4 Short description of ANS method

The ANS method was originally purely based on the engineering intuition, as proposed by Hughes and Tezduyar [26] for plate elements and later by Dvorkin and Bathe [27] for shell elements. As a matter of fact, the variational justification based on the Veubeke–Hu–Washizu mixed functional came after a few years from Militello and Felippa [28, 29]. Later, Betsch and Stein [30] exploited this method to relieve the trapezoidal locking in shells.

In the present solid-shell formulation, we employ the ANS interpolation on the transverse shear strains to circumvent the transverse shear locking, as proposed by Dvorkin and Bathe [27]. The four sampling points A, B, C and D are located at the four mid-points of the element edges at $\zeta = 0$ as shown in Fig. 2. The following interpolation functions defined in isoparametric coordinates are applied on the compatible transverse shear strains:

$$\begin{aligned} \gamma_{\xi\zeta}^{\text{ANS}} &= (1 - \eta) \gamma_{\xi\zeta}^{\text{A}} + (1 + \eta) \gamma_{\xi\zeta}^{\text{C}} \\ \gamma_{\eta\zeta}^{\text{ANS}} &= (1 - \xi) \gamma_{\eta\zeta}^{\text{D}} + (1 + \xi) \gamma_{\eta\zeta}^{\text{B}} \end{aligned} \quad (43)$$

where $\gamma_{\xi\zeta}^{\text{A}}$, $\gamma_{\eta\zeta}^{\text{B}}$, $\gamma_{\xi\zeta}^{\text{C}}$ and $\gamma_{\eta\zeta}^{\text{D}}$ are the transverse shear strains at sampling points A, B, C and D respectively, defined in isoparametric coordinates.

Similarly the ANS interpolation is applied on the transverse normal strain to relieve the curvature-thickness locking, as proposed by Betsch and Stein [30]. For this, the four

Table 1 Comparison of different fully integrated low-order solid-shell formulations

Formulation	Total EAS parameters	Thickness locking	In-plane response enhancement	Transverse shear locking	Trapezoidal locking	Bending patch test
Hauptmann and Schweizerhof [8]	4 EAS	4 EAS	Nil	ANS	Nil	No
Betsch et al. [7]	9 EAS	4 EAS	5 EAS	ANS	Nil	No
Miehe [9]	5 EAS	1 EAS	4 EAS	ANS	ANS	No
Klinkel et al. [16]	5/8/11 EAS	1/1/4 EAS	4/7/7 EAS	ANS	ANS	No
Klinkel et al. [17]	7 EAS	3 EAS	4 EAS	ANS	ANS	yes
de Sousa et al. [31]	12/18 EAS	1 EAS	5 EAS	6/12 EAS	Nil	No
Vu-Quoc and Tan [5]	7 EAS	3 EAS	4 EAS	ANS	ANS	yes

sampling points E, F, G and H are located at the four corners of the element middle surface, as shown in Fig. 2. The following linear interpolation function defined in isoparametric coordinates is applied on the compatible transverse normal strain:

$$\varepsilon_{\zeta\zeta}^{\text{ANS}} = \frac{1}{4} \left[(1 - \xi)(1 - \eta)\varepsilon_{\zeta\zeta}^{\text{E}} + (1 + \xi)(1 - \eta)\varepsilon_{\zeta\zeta}^{\text{F}} + (1 + \xi)(1 + \eta)\varepsilon_{\zeta\zeta}^{\text{G}} + (1 - \xi)(1 + \eta)\varepsilon_{\zeta\zeta}^{\text{H}} \right] \quad (44)$$

For the detailed description of the ANS method, refer to [27,30].

5 State of the art

Table 1 summarizes a set of selected well-known fully integrated low-order solid-shell formulations available in the literature, and the number of EAS parameters to resolve different element pathologies. It can be seen here that the EAS method has widely been successfully employed to resolve thickness locking problem in solid-shell formulations. The in-plane response enhancement using the EAS method serves here the purpose to improve the element accuracy with respect to the in-plane bending, and in case of the hyper-elastic and elastoplastic analyses, they also aim to treat the volumetric locking. It is to be noted that most of the low-order solid-shell elements treat the transverse shear and trapezoidal lockings by the ANS method, owing to its simplicity while remaining effective.

The solid-shell formulations from Hauptmann and Schweizerhof [8], Betsch et al. [7] and Miehe [9] employ the combination of EAS and ANS methods, but their proposed EAS parameters are not able to enrich the transverse normal strain field sufficiently to pass the out-of-plane bending patch test. Klinkel et al. [16] proposed three different solid-shell elements based on only the EAS method with different number of EAS parameters, namely 5, 8 and 11 EAS parameters, however, these elements are plagued with the transverse shear

locking and therefore cannot pass the out-of-plane bending patch test. Two solid-shell elements are proposed by de Sousa et al. [31] employing 12 and 18 EAS parameters to circumvent the volumetric and transverse shear locking, but no ANS is employed and the bending patch test is not fulfilled. The solid-shell formulation by Vu-Quoc and Tan [5] and Klinkel et al. [17] are the only fully integrated low-order solid-shell formulations in literature that are able to pass the out-of-plane bending patch test, employing the combination of the EAS and ANS methods with seven EAS parameters to alleviate the transverse shear and thickness locking issues successfully. However, the solid-shell formulation by Klinkel et al. [17] employs 13 additional assumed strain parameters and 13 assumed stress parameters (31 internal parameters in total), which are finally condensed at the element level.

Enhancing all the six strain components in (21) up to the trilinear polynomial in the EAS method, Andelfinger and Ramm [19] proposed the following matrix $\tilde{\mathbf{M}}^{\text{EAS30}}$ containing 30 EAS parameters in natural coordinates:

$$\tilde{\mathbf{M}}^{\text{EAS30}} = [\tilde{\mathbf{M}}_1 \tilde{\mathbf{M}}_2 \tilde{\mathbf{M}}_3] \quad (45)$$

where submatrices $\tilde{\mathbf{M}}_1$, $\tilde{\mathbf{M}}_2$ and $\tilde{\mathbf{M}}_3$ read as follows:

$$\tilde{\mathbf{M}}_1 = \begin{bmatrix} \xi & 0 & 0 & 0 & 0 & 0 & 0 & 0 & 0 \\ 0 & \eta & 0 & 0 & 0 & 0 & 0 & 0 & 0 \\ 0 & 0 & \zeta & 0 & 0 & 0 & 0 & 0 & 0 \\ 0 & 0 & 0 & \xi & \eta & 0 & 0 & 0 & 0 \\ 0 & 0 & 0 & 0 & 0 & \eta & \zeta & 0 & 0 \\ 0 & 0 & 0 & 0 & 0 & 0 & 0 & \xi & \zeta \end{bmatrix} \quad (46)$$

$$\tilde{\mathbf{M}}_2 = \begin{bmatrix} 0 & 0 & 0 & 0 & 0 & 0 & \xi\eta & \xi\zeta & 0 & 0 & 0 & 0 & 0 & 0 & 0 \\ 0 & 0 & 0 & 0 & 0 & 0 & 0 & 0 & \xi\eta & \eta\zeta & 0 & 0 & 0 & 0 & 0 \\ 0 & 0 & 0 & 0 & 0 & 0 & 0 & 0 & 0 & 0 & 0 & \xi\zeta & \eta\zeta & 0 & 0 \\ \xi\zeta & \eta\zeta & 0 & 0 & 0 & 0 & 0 & 0 & 0 & 0 & \xi\eta & 0 & 0 & 0 & 0 \\ 0 & 0 & \xi\eta & \xi\zeta & 0 & 0 & 0 & 0 & 0 & 0 & 0 & 0 & 0 & \eta\zeta & 0 \\ 0 & 0 & 0 & 0 & \xi\eta & \eta\zeta & 0 & 0 & 0 & 0 & 0 & 0 & 0 & 0 & \xi\zeta \end{bmatrix}$$

$$\tilde{\mathbf{M}}_3 = \begin{bmatrix} \xi\eta\zeta & 0 & 0 & 0 & 0 & 0 \\ 0 & \xi\eta\zeta & 0 & 0 & 0 & 0 \\ 0 & 0 & \xi\eta\zeta & 0 & 0 & 0 \\ 0 & 0 & 0 & \xi\eta\zeta & 0 & 0 \\ 0 & 0 & 0 & 0 & \xi\eta\zeta & 0 \\ 0 & 0 & 0 & 0 & 0 & \xi\eta\zeta \end{bmatrix} \quad (48)$$

The matrix $\tilde{\mathbf{M}}^{\text{EAS30}}$ in (45) expands the compatible strain field up to the complete trilinear field, which implies that the enhanced element has 54 modes in total, that is 24 compatible modes and 30 enhanced modes. However, an element formulation based solely on these 30 EAS parameters, e.g. the one by Klinkel and Wagner [20], cannot pass the out-of-plane bending patch test without a combination with the ANS method to remedy the shear-locking problem, as it will be shown later. The fully integrated low-order solid-shell formulation by Vu-Quoc and Tan [5] has been claimed to be the most accurate and efficient formulation available in the literature that passes the membrane patch test and out-of-plane bending patch test employing the following seven EAS parameters:

$$\tilde{\mathbf{M}}^{\text{EAS7}} = \begin{bmatrix} \xi & 0 & 0 & 0 & 0 & 0 & 0 \\ 0 & \eta & 0 & 0 & 0 & 0 & 0 \\ 0 & 0 & \zeta & \xi\zeta & \eta\zeta & 0 & 0 \\ 0 & 0 & 0 & 0 & 0 & \xi & \eta \\ 0 & 0 & 0 & 0 & 0 & 0 & 0 \\ 0 & 0 & 0 & 0 & 0 & 0 & 0 \end{bmatrix} \quad (49)$$

However, the seven EAS parameters proposed by Vu-Quoc and Tan [5] are not optimal and the resulting solid-shell element shows volumetric locking and sensitivity for mesh distortions, as will be shown later.

6 Optimal EAS parameters

A systematic numerical experimentation has been carried out to find the optimal EAS parameters to address the following element issues exploiting the EAS method:

- (i) sufficient condition for the element convergence employing the membrane patch test and out-of-plane bending patch test;
- (ii) thickness locking;
- (iii) mesh distortion sensitivity;
- (iv) volumetric locking.

In order to avoid the numerical integration order higher than $2 \times 2 \times 2$ for the low-order solid-shell formulations, which leads to computational inefficiency, we search for the optimal EAS parameters within the trilinear function space, as proposed by Andelfinger and Ramm [19] in (45). The most important finding of our study is that only three EAS parameters are needed to enrich the transverse normal strain com-

ponent to assure the element convergence and resolve the thickness locking problem, and to pass the membrane patch test and out-of-plane bending patch test. These three EAS parameters are given as follows:

$$\tilde{\mathbf{M}}^{\text{EAS3}} = \begin{bmatrix} 0 & 0 & 0 \\ 0 & 0 & 0 \\ \zeta & \xi\zeta & \eta\zeta \\ 0 & 0 & 0 \\ 0 & 0 & 0 \\ 0 & 0 & 0 \end{bmatrix} \quad (50)$$

A solid-shell element based on these three EAS parameters and the ANS method, the so-called EAS3ANS element, shows excellent convergence behaviour and passes both membrane and out-of-plane bending patch tests, is free from thickness and transverse shear locking, performs well under high element aspect ratios (6667) and its numerical performance is comparable to the solid-shell element with 30 EAS parameters (e.g. by Klinkel and Wagner [20]) and the well-known solid-shell element by Vu-Quoc and Tan [5] with 7 EAS parameters. Similar to the solid-shell element by Vu-Quoc and Tan [5] with seven EAS parameters, which is claimed to be appropriate for the analysis of multilayer composites, EAS3ANS element is also suitable for the analysis of multilayer composites due to its excellent performance, where incompressibility is not an issue.

In (near) incompressible analyses, e.g. in hyperelastic or elastoplastic analyses, volumetric locking can be a critical issue. Both EAS3ANS and the solid-shell element by Vu-Quoc and Tan [5] suffer slightly from the volumetric locking, as it will be shown later from the eigenvalue analysis. Our investigation shows that the addition of four EAS parameters in the in-plane normal strain field of the EAS3ANS element alleviates the volumetric locking in this element completely. This leads to the following seven EAS parameters:

$$\tilde{\mathbf{M}}^{\text{EAS7}} = \begin{bmatrix} 0 & 0 & 0 & \xi & \xi\eta & 0 & 0 \\ 0 & 0 & 0 & 0 & 0 & \eta & \xi\eta \\ \zeta & \xi\zeta & \eta\zeta & 0 & 0 & 0 & 0 \\ 0 & 0 & 0 & 0 & 0 & 0 & 0 \\ 0 & 0 & 0 & 0 & 0 & 0 & 0 \\ 0 & 0 & 0 & 0 & 0 & 0 & 0 \end{bmatrix} \quad (51)$$

The corresponding solid-shell element based on these seven EAS parameters, the so-called EAS7ANS1 element, shows excellent convergence behaviour and passes both membrane and out-of-plane bending patch tests, and is also free from volumetric locking.

Both EAS3ANS and EAS7ANS elements, and also the solid-shell element by Vu-Quoc and Tan [5], behave very well for distorted coarse meshes, as it will be shown later in the numerical testing. However, in highly distorted coarse meshes, their performance can be somewhat affected by the high level of mesh distortion. In order to enhance the

performance of a solid-shell element under highly distorted coarse meshes, our numerical study reveals that the introduction of additional four EAS parameters in the in-plane strain field of an EAS3ANS element can be effective. The corresponding seven EAS parameters can be read as:

$$\tilde{\mathbf{M}}^{\text{EAS7}'} = \begin{bmatrix} 0 & 0 & 0 & \xi\zeta & 0 & 0 & 0 \\ 0 & 0 & 0 & 0 & \eta\zeta & 0 & 0 \\ \zeta & \xi\zeta & \eta\zeta & 0 & 0 & 0 & 0 \\ 0 & 0 & 0 & 0 & 0 & \xi\zeta & \eta\zeta \\ 0 & 0 & 0 & 0 & 0 & 0 & 0 \\ 0 & 0 & 0 & 0 & 0 & 0 & 0 \end{bmatrix} \quad (52)$$

The corresponding solid-shell element based on these seven EAS parameters, the so-called EAS7ANS2 element, shows excellent convergence behaviour and passes both membrane and out-of-plane bending patch tests, being almost insensitive to highly distorted coarse meshes

7 Numerical examples

In this section we assess the numerical performance of the proposed solid-shell elements for a variety of shell/solid-shell benchmark problems available in the literature. In this regard, we particularly focus on the element patch tests providing the sufficient condition for the element convergence, the issue of mesh distortions sensitivity, high element length-to-thickness aspect ratios, geometric nonlinear shell problems and thickness and volumetric locking problems. The following abbreviations for the different elements will be employed:

- Standard 8-node displacement based fully integrated solid element—Q1
- Enhanced solid element based on 30 EAS parameters proposed by Klinkel and Wagner [20]—KW30
- Solid-shell element by Vu-Quoc and Tan [5] based on the EAS method with seven EAS parameters and ANS formulation—VQ7
- Solid-shell element by Klinkel et al. [17] based on the EAS method with 7 EAS parameters, 13 assumed strain parameters, 13 assumed stress parameters and ANS formulation—HSEE
- Fully integrated and mixed interpolated bilinear element proposed by Dvorkin and Bathe [27]—MITC4

The numerical results will be compared with the reference results (analytical or numerical) available in literature.

7.1 Membrane patch test

This test was originally proposed by MacNeal and Harder [32] and originally aimed to check the membrane behavior of plate and shell elements. In order to adapt to the 3D topology of solid-shell elements, the number of nodes has been

doubled as shown in Fig. 3. The material parameters for the plate are taken as: $E = 10^6$ and $\nu = 0.25$.

The following displacements u , v and w (along the x , y and z axes, respectively) are imposed on the boundary nodes of the plate:

$$u = 10^{-3} \left[x + \frac{y}{2} \right], v = 10^{-3} \left[y + \frac{x}{2} \right], w = 0 \quad (53)$$

The theoretical solution of the constant in-plane stress field in all the elements is given as:

$$\sigma_{xx} = \sigma_{yy} = 1333, \tau_{xy} = 400 \quad (54)$$

Table 2 shows the result of the different element formulations for the membrane patch test. It can be seen here that all elements, including the standard 8-node solid element Q1, pass the membrane patch test, which fulfills the basic condition for the element convergence.

7.2 Bending patch test

This test was also suggested by MacNeal and Harder [32] and originally aimed to check the out-of-plane bending behavior of plate and shell elements. Same geometry, discretization and material parameters are employed as in the membrane patch test. The following displacements are imposed on the boundary nodes to construct a constant bending stress state in the out-of-plane bending load:

$$u = \pm 10^{-3} \left[x + \frac{y}{2} \right] \frac{h}{2}, \\ v = \pm 10^{-3} \left[y + \frac{x}{2} \right] \frac{h}{2}, \quad w = 10^{-3} \frac{x^2 + xy + y^2}{2} \quad (55)$$

The theoretical solution of the constant stress field at the outer surfaces of the plate is given by:

$$\sigma_{xx} = \sigma_{yy} = \pm 0.667, \tau_{xy} = \pm 0.200 \quad (56)$$

In order to pass this test, the element formulation must be free from the transverse shear and thickness locking phenomena. Different element formulations in Table 3 are checked for the out-of-plane bending patch test, where it can be seen that the standard solid element Q1 and enhanced solid element based on 30 EAS parameters (KW30) are not able to pass this test, thereby indicating the presence of locking problems. On the other hand, the EAS3ANS solid-shell element passes this test with only three EAS parameters, as well as the EAS7ANS1, EAS7ANS2, VQ7 and HSEE solid-shell elements.

7.3 Morley's 30° skew plate

This plate problem is investigated to check the sensitivity of the formulation to mesh distortions, as well as the ability to avoid the locking phenomenon, as originally proposed by Morley [33]. The plate geometry has a high

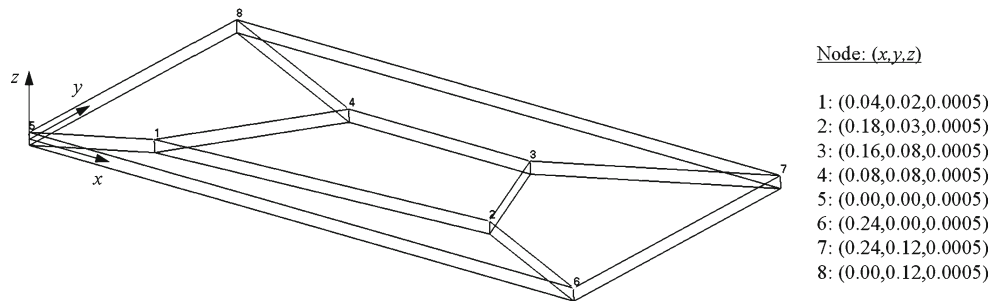


Fig. 3 The five element membrane patch test: geometric dimensions ($x:y:z = 0.24:0.12:0.001$)

Table 2 Membrane patch test—comparison of different element formulations

Element	Q1	KW30	VQ7	HSEE	EAS3ANS	EAS7ANS1	EAS7ANS2
Membrane patch test	Pass	Pass	Pass	Pass	Pass	Pass	Pass

Table 3 Bending patch test—comparison of different element formulations

Element	Q1	KW30	VQ7	HSEE	EAS3ANS	EAS7ANS1	EAS7ANS2
Bending patch test	fail	fail	Pass	Pass	Pass	Pass	Pass

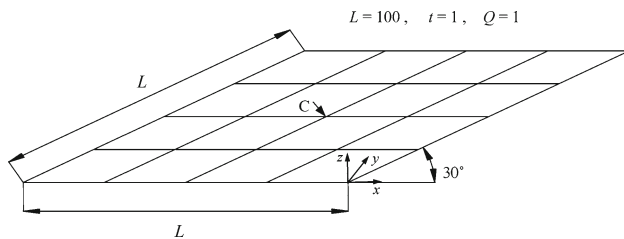


Fig. 4 Morley's 30° skew plate (4×4 mesh): material properties ($E = 100000$, $\nu = 0.3$)

length-to-thickness ratio ($L/t = 100$) and the elements are uniformly distorted with a skew angle of 30°, as depicted in Fig. 4. The plate is simply supported at its four edges and subjected to a uniform pressure Q . The problem data is the same as employed by Andelfinger and Ramm [19].

Morley calculated the central deflection of the plate employing the Kirchhoff's plate theory, i.e. the deflection of the point C in the plate to be 4.455. However, transverse shear effects cannot be neglected for the present length-to-thickness ratio of 100. Andelfinger and Ramm [19] have taken into account the transverse shear effects in the present problem and reported the central deflection of the plate to be 4.64, which will be used as the reference solution in this example.

The results of this problem are summarized in Table 4. It can be seen in this table that the standard displacement-based solid element Q1 is severely affected by the mesh

distortions and does not provide sufficiently accurate results for very fine meshes. The KW30 element shows relatively less sensitivity to mesh distortions compared with the VQ7, MITC4, EAS3ANS and EAS7ANS1 elements for coarse meshes, however, at the expense of a much higher computational cost due to 30 EAS parameters. On the other hand, the EAS7ANS2 element shows better results for highly distorted coarse meshes compared to the VQ7, MITC4, EAS3ANS and EAS7ANS1 elements. It should be noted that the accuracy of the EAS7ANS2 and KW30 is comparable, although it is worth mentioning that the EAS7ANS2 element employs only 7 EAS parameters compared to the KW30 element with 30 EAS parameters.

7.4 Eigenvalue analysis of an incompressible cube

In order to estimate the behavior of the proposed formulations in the nearly incompressible limit we investigate the eigenvalues of an undeformed unit cube, as proposed by Andelfinger and Ramm [19]. The elastic modulus $E = 1.0$ and the Poisson's ratio $\nu = 0.4999$ are used.

Table 5 shows the 18 eigenvalues corresponding to the element deformation modes together with the results of the other formulations in literature. The six zero eigenvalues corresponding to the six rigid body modes of the element are not shown. For a volumetric-locking free behaviour, the elements should contain only one eigenvalue that tends to infinity, i.e. the eigenvalue corresponding to the dilatation mode

Table 4 Morley's skew plate vertical central deflection

Elements per side	4×4	8×8	16×16	32×32	64×64
Q1	0.0958	0.3187	0.8165	1.5760	2.9745
KW30	4.2157	4.2498	4.4154	4.5406	4.6049
VQ7	3.9163	3.8815	4.1772	4.4358	4.5487
EAS3ANS	3.9163	3.8814	4.1768	4.4351	4.5476
EAS7ANS1	3.9172	3.8829	4.1797	4.4411	4.5508
EAS7ANS2	4.2108	4.2163	4.3684	4.5073	4.5974
MITC4	3.9182	3.8991	4.1875	4.4098	—
Reference	4.64	4.64	4.64	4.64	4.64

Table 5 Eigenvalues of a unit cube for near incompressibility

Mode	Q1	KW30	VQ7	EAS3ANS	EAS7ANS1	EAS7ANS2
1	0.056	0.056	0.056	0.056	0.056	0.056
2	0.056	0.056	0.056	0.056	0.056	0.056
3	0.167	0.056	0.093	0.093	0.074	0.056
4	0.167	0.056	0.093	0.093	0.093	0.056
5	0.167	0.056	0.111	0.111	0.093	0.111
6	0.222	0.111	0.111	0.139	0.111	0.139
7	0.333	0.111	0.111	0.139	0.135	0.139
8	0.333	0.111	0.167	0.222	0.135	0.222
9	0.333	0.167	0.167	0.333	0.222	0.333
10	0.333	0.167	0.222	0.333	0.333	0.333
11	0.333	0.222	0.333	0.333	0.333	0.333
12	92.654	0.333	0.333	0.333	0.333	0.333
13	92.654	0.333	0.333	0.333	0.333	0.333
14	92.654	0.333	0.333	0.333	0.333	0.333
15	555.650	0.333	0.333	92.617	0.333	92.617
16	555.650	0.333	0.333	555.620	0.364	555.620
17	555.650	0.333	92.617	555.620	0.364	555.620
18	2500.000	2500.000	2500.000	2500.000	2500.000	2500.000

(mode 18 in Table 5). It can be seen in Table 5 that the standard displacement-based element Q1 as well as the VQ7, EAS3ANS and EAS7ANS2 elements are affected by the volumetric locking, where the eigenvalues corresponding to the deviatoric deformation modes (modes 12–17) tend to infinity. However, the KW30 and EAS7ANS1 elements are free from this pathology. This proves the volumetric locking free behaviour of the proposed EAS7ANS1 elements that can be readily employed for the nearly incompressible analyses.

7.5 Clamped square plate with concentrated load

In this example we examine the performance of the presented solid-shell formulations under several critical conditions, i.e.

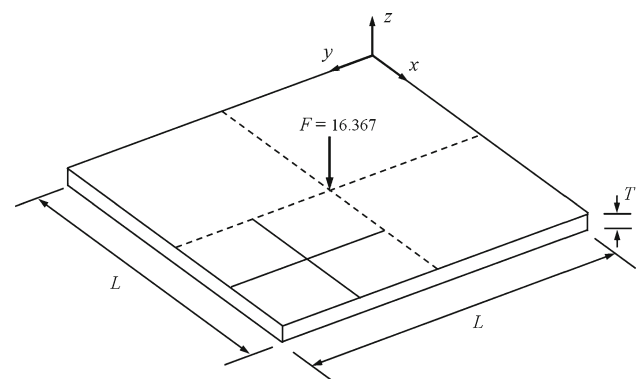
**Fig. 5** Clamped square plate (2×2 mesh): material properties ($E = 10000$, $\nu = 0.3$)

Table 6 Normalized central transverse deflection for the clamped square plate

L/T	Mesh	Kirchhoff	Q1	KW30	VQ7	EAS3ANS	EAS7ANS1	EAS7ANS2
100	2×2	1.000	0.007	0.888	0.868	0.868	0.869	0.888
	4×4	1.000	0.025	0.976	0.969	0.969	0.969	0.976
1000	2×2	1000	<0.001	0.886	0.866	0.866	0.867	0.886
	4×4	1000	<0.001	0.973	0.966	0.966	0.968	0.973
6667	2×2	296341	<0.001	0.887	0.865	0.865	0.866	0.885
	4×4	296341	<0.001	0.972	0.968	0.967	0.966	0.974

Table 7 Change of the normalized central deflection with increasing distortion parameter Δ (2×2 mesh)

Δ	0	2.5	5	7.5	10	12.5
Q1	0.007	0.007	0.008	0.008	0.009	0.009
KW30	0.888	0.629	0.368	0.235	0.162	0.118
VQ7	0.868	0.864	0.852	0.834	0.810	0.778
HSEE	0.885	0.880	0.860	0.815	0.785	0.710
EAS3ANS	0.868	0.864	0.852	0.834	0.810	0.778
EAS7ANS1	0.869	0.865	0.852	0.835	0.811	0.779
EAS7ANS2	0.888	0.884	0.871	0.853	0.831	0.826

extremely high aspect ratios and locking issues. A square plate of $L \times L$ in-plane dimensions and T thickness is subjected to a concentrated load and clamped at all four sides as shown in Fig. 5. Two meshes (2×2 and 4×4 elements) are investigated to model one quadrant of the plate exploiting the double-symmetry. In order to check the locking behavior of the proposed formulations under high length-to-thickness aspect ratios ($S = L/T$), we investigate the transverse central deflection of the plate for different aspect ratios and meshes.

The numerical results of the proposed formulations together with the other formulations in literature are normalized using the Kirchhoff plate solution and compared in Table 6. It can be seen from the Table 6 that the displacement-based solid element is severely plagued by the thickness and transverse shear lockings, and therefore provides useless results. On the other hand, the reference and newly proposed formulations provide good results even for coarse meshes for a wide range of element aspect ratios, without any sign of thickness and transverse shear lockings. All elements show good behavior even for the extremely thin plate configuration ($S = 6667$). However, the VQ7 element by Vu-Quoc and Tan [5] and EAS3ANS provide the same accurate results, which proves the accuracy of the EAS3ANS element with an improved computational efficiency, owing to the employment of only three EAS parameters. This can make this element suitable for the analysis of thin multilayer composites.

The influence of the mesh distortion on the numerical results is summarized in Table 7. In this study we use a 2×2

mesh, $L = 100$ and $S = 100$. For the HSEE element, results for different mesh distortion levels are inter- and extrapolated from [17]. It can be seen from this comparison that the proposed solid-shell elements, especially the EAS7ANS2 formulation, show a higher insensitivity to different levels of mesh distortion. Even for very extreme mesh distortion ($\Delta = 12.5$) the results of the EAS7ANS2 element are quite reasonable and better than other formulations with a higher number of enhancing parameters.

7.6 Geometrically nonlinear cantilever plate

In order to confirm the limit of maximum element length-to-thickness aspect ratio (6667) in geometrically nonlinear domain, for which the proposed formulations provide accurate results, we investigate a fixed cantilever plate under load F that is subjected to large deformation [5], as shown in Fig. 6. The length of the plate is $L = 10$ and width $b = 1$. The plate is discretized employing a 10×1 mesh. Five different plate thicknesses h (1, 0.1, 0.01, 0.002, 0.0015) are considered, which corresponds to five different aspect ratios L/h (10, 100, 1000, 5000, 6667), respectively. In order to have the same level of deflection magnitude irrespective of the aspect ratios L/h , the applied load F is adjusted according to the plate thickness h ($F = 5 \times 10^4 h^3$).

The deformed mesh of the cantilever plate under the maximum load level is shown in Fig. 7 (no magnification of deformation) using the EAS3ANS elements for $L/h = 1000$, where it can be seen that the plate is subjected to large deformation. The transverse displacement of the mid-surface at the

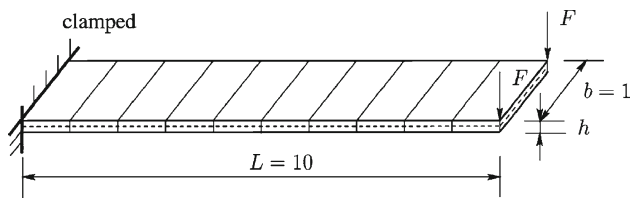


Fig. 6 Out-of-plane bending: geometry and mesh of cantilever plate [5]

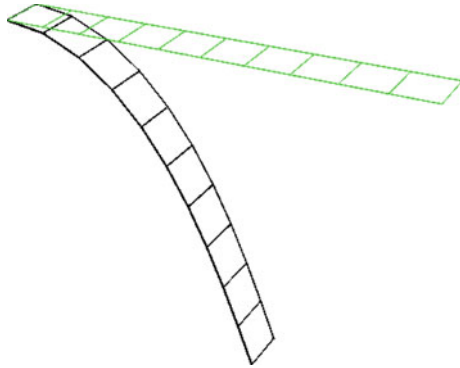


Fig. 7 Cantilever plate: undeformed and deformed mesh for $L/h = 1000$ with EAS3ANS elements

Table 8 Cantilever plate: end deflection for wide range of element aspect ratios (L/h)

Element	$L/h = 10$	$L/h = 100$	$L/h = 1000$	$L/h = 5000$	$L/h = 6667$
Q1	7.8689	0.5509	0.0056	0.0002	0.0001
KW30	7.5084	7.1338	5.5837	2.2276	1.1432
VQ7	7.5299	7.4219	7.4204	7.4192	7.4145
EAS3ANS	7.5271	7.4219	7.4203	7.4193	7.4145
EAS7ANS1	7.5299	7.4219	7.4203	7.4193	7.4146
EAS7ANS2	7.5392	7.4334	7.4318	7.4211	7.4193
Geometrically exact shell element [5]	7.4897	7.4144	7.4137	–	–

free-end of the plate is summarized for different formulations in Table 8, where the geometrically exact shell element with selectively reduced integration [5] is used as reference. It is evident from this comparison that the displacement-based solid element Q1 and KW30 element do not provide accurate results for higher aspect ratios L/h . On the other hand, the proposed solid-shell elements are in good agreement with the reference solution. It should be noted that the performance of the EAS3ANS element is comparable to the VQ7 element.

7.7 Scordelis–Lo roof problem

In this example a cylindrical shell, supported at the rigid diaphragms in the curved edges with radius R , length L and

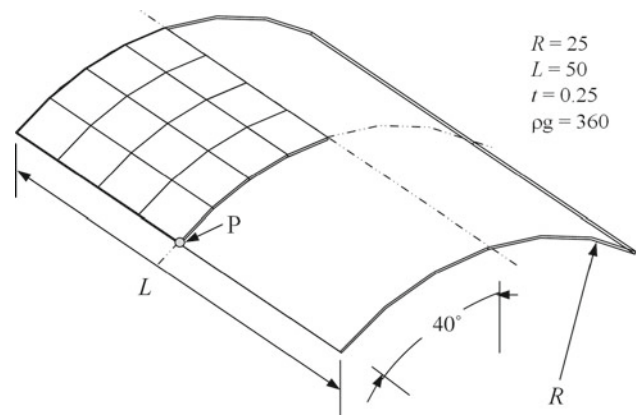


Fig. 8 Scordelis–Lo roof with rigid diaphragms: material properties ($E = 4.32 \times 10^8$, $\nu = 0.0$)

Table 9 Scordelis–Lo roof normalized deflection at roof centre (point P)

Elements per side	4×4	8×8	16×16	32×32
Q1	0.063	0.123	0.259	0.534
KW30	1.024	0.998	0.991	1.004
VQ7	1.044	0.998	0.990	1.004
EAS3ANS	0.957	0.983	0.998	1.002
EAS7ANS1	0.958	0.983	0.999	1.002
EAS7ANS2	0.959	0.983	0.998	1.003

thickness t is analyzed (see Fig. 8), as originally proposed by Scordelis and Lo [34]. The shell is subjected to its own weight, i.e. dead load, leading to a membrane-dominated problem. Such structures are commonly used as arched roofs of aircraft hangers supported only at their curved edges in a rigid manner. The geometry of this problem is such that the centre of the roof edge, i.e. the point P in Fig. 8, deforms upwards under the applied loading.

Only one-quarter of the problem domain is modelled exploiting the symmetry, as shown in Fig. 8, where geometric properties of this problem are also outlined. Four different meshes, i.e. 4×4 , 8×8 , 16×16 and 32×32 , are employed to discretize the element domain and study the convergence behaviour. The vertical displacement of the centre of the roof edge (point P) is investigated and normalized using the reference solution of 0.3024, as reported by Belytschko and Leviathan [35].

The results of the different element formulations are summarized in Table 9, where it can be seen that all the elements, except the purely displacement-based solid element Q1, perform regularly, even for very coarse meshes.

7.8 Geometrical nonlinear pinched hemispherical shell

The pinched hemispherical shell problem is one of the most severe benchmark problems for the geometrically nonlinear

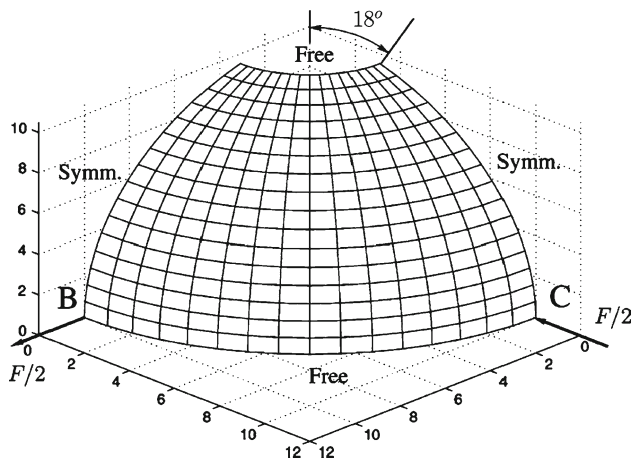


Fig. 9 Pinched hemispherical shell: one quadrant of the hemisphere with 18° hole [5]

Table 10 Pinched hemispherical shell: large-deformation displacements at maximum load level ($F = 5$)

Element	u at point B	u at point C
Q1	0.00985	0.00985
KW30	3.16811	5.47301
VQ7	3.26055	5.48331
EAS3ANS	3.24706	5.43642
EAS7ANS1	3.25122	5.44693
EAS7ANS2	3.24811	5.43786
Four-node shell element [37]	3.24803	5.43434
Eight-node shell element [37]	3.32798	5.84238

analysis of shells [5, 36], and will be employed in this section to check the performance of different elements in the geometrically nonlinear domain. The hemispherical shell has an 18° hole at the top and it is subjected to two pairs of loads, where the first pair of loads is acting inwards at 0° and at 180° longitude on the equator and the second pair of loads is acting outwards at 90° and 270° longitude on the equator, as shown in Fig. 9. Due to symmetry, only one quadrant of the shell is analyzed employing a mesh of 16×16 . Material properties consist of Young's modulus $E = 6.825 \times 10^7$ and

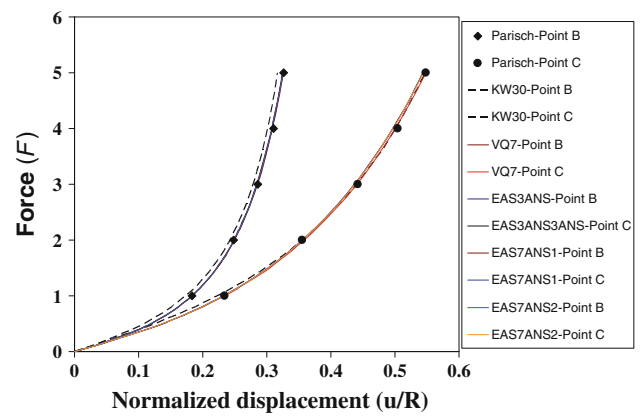


Fig. 11 Pinched hemispherical shell: load-deflection curves for different elements

Poisson ratio $\nu = 0.3$. The radius is $R = 10$, thickness is $h = 0.01$ and $F = 5$.

The deformed mesh of the pinched hemispherical shell under the maximum load level is shown in Fig. 10 (no magnification of deformation) using the EAS3ANS elements, where it can be seen that the hemisphere is subjected to large deformation. The same problem was also investigated by Parisch [37] employing four- and eight-node degenerated shell elements, which will be used as a reference to check the performance of different elements. Table 10 summarizes the displacement of the hemisphere at different points for different formulations.

It can be observed from this table that the proposed solid-shell elements perform comparable to the VQ7 element and four-node degenerated shell element by Parisch [37]. Load-deflection curves are shown in Fig. 11, where all the formulations provide similar accurate results, except the Q1 and KW30 elements, as those reported by Parisch [37] for four-node degenerated shell element. This proves the accuracy of the proposed solid-shell elements in the geometrically nonlinear domain.

In order to check the performance of different elements for geometrically nonlinear problems, the convergence rate of the equilibrium iteration has been investigated and

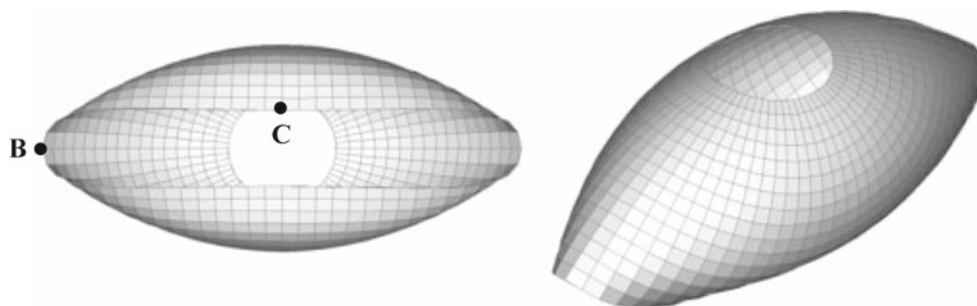


Fig. 10 Pinched hemispherical shell: deformed mesh at maximum load level ($F = 5$)

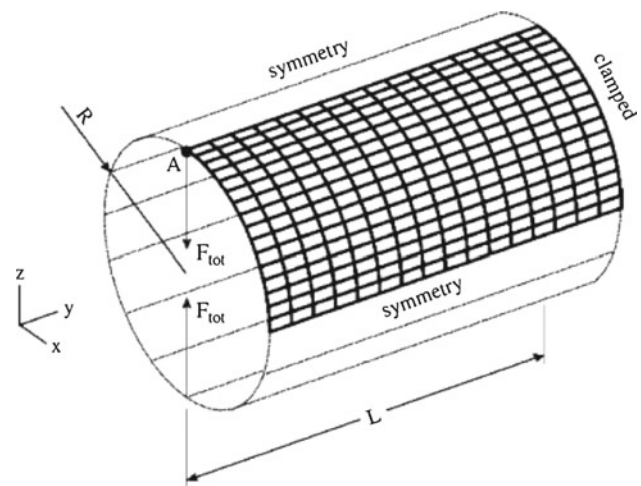
Table 11 Comparison of number of load increments and iterations for different formulations and load levels

Element	$F = 0.25$	$F = 5$
EAS3ANS	8, 9 (17)	48 inc. (232)
EAS7ANS1	8, 9 (17)	48 inc. (232)
EAS7ANS2	8, 9 (17)	40 inc. (208)
VQ7	8, 9 (17)	40 inc. (207)
KW30	7, 7 (14)	37 inc. (181)
HSEE	5 (5)	1 inc. (10)

summarized in Table 11. The first five elements in this table are implemented in the user-defined element subroutine of Abaqus where the Newton procedure is employed to seek the equilibrium state for a given load level. For load $F = 0.25$, the maximum load level is applied in two equal load steps, and the corresponding iterations are compared in Table 11. It can be seen from this comparison that the proposed solid-shell formulations require the same number of total iterations to find equilibrium as the VQ element. On the other hand, the HSEE element shows better performance, however on the expense of 31 internal parameters. For load $F = 5$, the maximum load level for first five elements in Table 11 is achieved by using the fully automatic Newton scheme in Abaqus. Here the total number of load increments and iterations are compared to determine the equilibrium. It can be seen from this comparison that for highly geometrical nonlinear problems, the performance of the VQ7 element is little better than the EAS3ANS and EAS7ANS1 elements, however comparable to the EAS7ANS2 element. On the other hand, the HSEE element shows again excellent performance, however on the expense of 31 internal parameters. As a matter of fact, to compare the efficiency of proposed solid-shell elements with the HSEE solid-shell element, not only the total number of iterations but also the total CPU time to accomplish these iterations should be compared, as the HSEE element is much more complex than a standard EAS- and ANS-based solid-shell element due to its mixed type of variational formulation.

7.9 Geometrically nonlinear pinching of a clamped cylinder

This example demonstrates the ability of a shell/solid-shell formulation in the geometrically nonlinear domain, where an elastic cylindrical shell, fully clamped at one end, is subjected to a pair of concentrated loads at its free end. Following the references, investigating the same problem employing shell and solid-shell elements [38–40], a regular mesh of 16×16 elements is employed to discretize one quadrant of the cylinder exploiting double symmetry, as shown in Fig. 12. Material properties consist of Young's modulus $E = 2.0685 \times 10^7$ and Poisson ratio $\nu = 0.3$. The length of the cylinder is $L = 3.048$, mean radius is $R = 1.016$

**Fig. 12** Pinching of a clamped cylinder**Table 12** Pinching of a clamped cylinder: large-deformation displacements at maximum load level ($F=1600$)

Element	Vertical displacement of point A
Q1	0.70729
KW30	1.55878
VQ7	1.60492
EAS3ANS	1.60351
EAS7ANS1	1.60367
EAS7ANS2	1.60518
Brank et al. [40]	1.60800

and thickness is $a = 0.03$. The maximum nominal load is $F_{tot} = 1600$.

The deformed shape under the maximum load level is shown in Fig. 13 using the EAS3ANS elements (no magnification of deformation), where it can be seen that the cylinder is subjected to large deformation. The same problem was also investigated by Brank et al. [40] employing four-node degenerated shell elements, which will be used as a reference to check the performance of different elements. The vertical displacement of the point A (see Fig. 12) predicted by different formulations at the maximum load level are summarized in Table 12. It is evident from this comparison that all the proposed solid-shell elements perform excellent in the geometrically nonlinear domain. Again the performance of the EAS3ANS element is comparable with that of the VQ7 element. The load-deflection curves are shown in Fig. 11, where all the formulations provide similar accurate results, except the Q1 and KW30 elements, as those reported by Brank et al. [40] for four-node degenerated shell elements. This proves the accuracy of the proposed solid-shell elements in the geometrically nonlinear domain (Fig. 14).

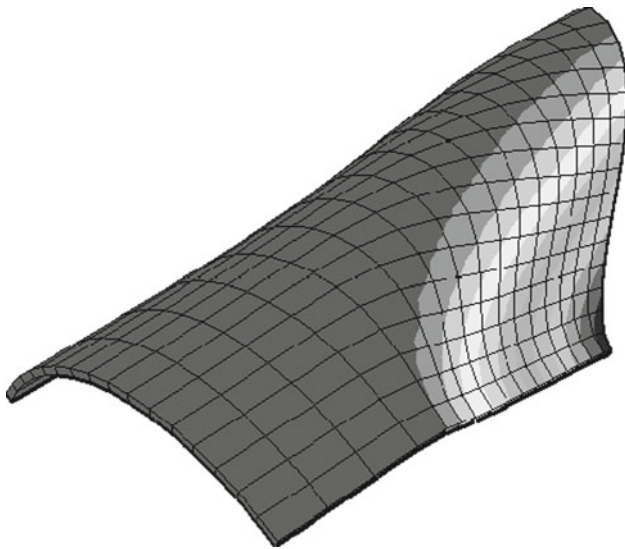


Fig. 13 Pinching of a clamped cylinder—deformed configuration at maximum load level

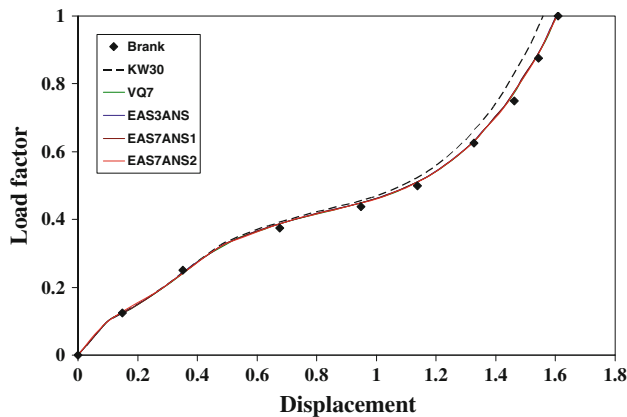


Fig. 14 Pinching of a clamped cylinder—vertical displacement of point A

7.10 Two-layer composite square plate

In this example we investigate an anti-symmetric two-ply composite square plate, clamped on all sides and subjected to a uniformly distributed transverse loading on its top surface, for different angle-ply laminate layups. The closed form solution for the central deflection of this problem has been given by Whitney [41] exploiting the double Fourier series expansion of the load, which will be considered as reference solution to check the accuracy of different solid-shell elements.

The square plate has side lengths $L = 20$ and the ply thickness $T_l = 0.01$, with the total plate thickness $T = 0.02$, as shown in Fig. 15 where the thickness direction has been magnified 100 times to make it visible. The plate model needs to be modelled without symmetry conditions due the stretch-

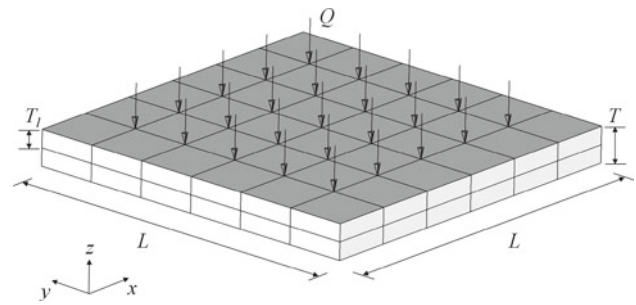


Fig. 15 Two-layer composite square plate under uniformly distributed transverse loading

ing-bending coupling in the laminate. A mesh of $6 \times 6 \times 2$ elements is employed, where each ply is modelled using one element in the thickness direction, as shown in Fig. 15. The magnitude of the uniformly distributed transverse loading is taken as $Q = 1$. Considering the one-direction along the fibres and two- and three-directions transverse to the fibres in a ply, following material properties are used:

$$E_{11} = 40 \times 10^6; E_{22} = 1 \times 10^6; E_{33} = 1 \times 10^6;$$

$$\nu_{12} = \nu_{23} = \nu_{13} = 0.25; G_{12} = G_{23} = G_{13} = 0.5 \times 10^6$$

The numerical results for the transverse displacement of the plate center for different element formulations and laminate layups are listed in Table 13, where the high-order hybrid multilayer shell element (HS) by Spilker and Jakobs [42] has also been considered. It can be seen from this table that the relative error in numerical results for all element formulations increases with the decrease of ply angle θ , and the proposed solid-shell formulations, even with three EAS parameters, provide very accurate results for different laminate layups.

As high element aspect ratios (L/T_l) are required for the modeling of composite laminates, we also investigate the performance of proposed solid-shell elements for high element aspect ratios by decreasing the plate thickness. In order to use the same reference solution for the plate central deformation for different plate thicknesses, the applied loading has been adjusted accordingly. A two-layer $\pm 45^\circ$ laminate is considered in this investigation.

The results for different element formulations with increasing aspect ratios have been summarized in Table 14, where the accuracy of the proposed solid-shell elements can be seen even for very high element aspect ratios. Again, the EAS3ANS solid-shell element with three EAS parameters performs similarly accurate as the solid-shell element by Vu-Quoc and Tan [5] with seven EAS parameters, but with enhanced computational efficiency. This proves the suitability of the proposed solid-shell elements for the analysis of very thin multilayer composites.

Table 13 Two-layer composite plate–transverse displacement at plate centre

Laminate layup	$\pm 45^\circ$		$\pm 35^\circ$		$\pm 25^\circ$		$\pm 15^\circ$	
	w	Relative error (%)	w	Relative error (%)	w	Relative error (%)	w	Relative error (%)
Q1	0.03	99.95	0.03	99.95	0.03	99.95	0.03	99.95
KW30	60.2	4.15	57.95	4.87	51.18	8.67	38.72	14.49
VQ7	58.92	1.95	56.75	2.71	50.22	6.62	38.15	12.80
HS	58.58	1.35	56.88	2.93	51.44	9.21	40.18	18.81
EAS3ANS	58.87	1.85	56.70	2.61	50.18	6.54	38.13	12.76
EAS7ANS1	58.89	1.87	56.72	2.66	50.23	6.65	38.15	12.84
EAS7ANS2	60.13	4.04	57.87	4.73	51.08	8.44	38.61	14.18
Reference	57.80	–	55.26	–	47.10	–	33.82	–

Table 14 Two-layer composite plate–transverse displacement at plate centre for different plate aspect ratios (ply-angle $\pm 45^\circ$)

L/T_l	1000		10000		20000	
	w	Relative error (%)	w	Relative error (%)	w	Relative error (%)
Q1	0.12	99.79	<0.01	100	<0.01	100
KW30	60.22	4.18	60.18	4.12	60.89	5.35
VQ7	58.92	1.95	58.91	1.93	57.54	0.44
EAS3ANS	58.88	1.88	58.87	1.86	58.90	1.90
EAS7ANS1	58.89	1.89	58.91	1.90	58.57	1.30
EAS7ANS2	60.15	4.07	60.19	4.13	60.36	4.42
Reference	57.80	–	57.80	–	57.80	–

8 Closing Remarks

In the present paper we presented different optimal low-order fully integrated solid-shell elements that can be employed to analyze different types of structural analyses. A numerical study provided the optimal EAS parameters to enhance the performance of proposed solid-shell formulations and to alleviate different types of numerical pathologies like the thickness, shear and volumetric lockings, mesh distortion sensitivity, in the proposed formulations. The present study shows that a combination of ANS method and EAS methods, with only three EAS parameters, can lead to a fully integrated low-order solid-shell element (EAS3ANS element), which passes both the membrane and out-of-plane bending patch tests, providing the sufficient condition for the element convergence, and showing no sign of thickness and transverse shear lockings as well as good behaviour under extremely high element aspect ratios. The EAS3ANS element can be efficiently employed for the analysis of thin multilayer composite structures where material incompressibility, and therefore volumetric locking, is not an issue.

For near incompressible problems where solid-shell elements can additionally be plagued by the volumetric locking, it is shown that four additional EAS parameters are needed

to alleviate this pathology in the EAS3ANS element. The introduction of these additional four EAS parameters in the EAS3ANS leads to the so-called EAS7ANS1 element, which proved to be completely free from locking problems and can be employed for the analyses of near incompressible materials.

Additionally, to improve the accuracy of analyses involving highly distorted coarse meshes, the inclusion of four other EAS parameters in the EAS3ANS element can lead to a distinct solid-shell formulation (EAS7ANS2 element) with improved accuracy for highly distorted coarse meshes, thereby making it attractive for the engineering industrial sector where relatively coarse and irregular meshes are usually used due to the time limitations. The comparison of the proposed solid-shell elements with state-of-the-art solid-shell formulations in the literature, employing a variety of geometrically linear and nonlinear shell/solid-shell benchmark problems, has shown the accuracy of the proposed formulations.

Acknowledgements The authors would like to acknowledge the support of the Fund for Scientific Research—Flanders (FWO-Vlaanderen), the Interuniversity Attraction Poles Program phase 6 (IUAP) of the Federal Science Policy of Belgium and the partners of IUAP-VI (www.m3phys.be) and the Portuguese Science Foundation PTDC/EME-

TME/098845/2008. As Research Director of Scientific Research Fund F.R.S-FNRS Wallonia, AM Habraken thanks this Fund.

References

1. Reese S (2006) A large deformation solid-shell concept based on reduced integration with hourglass stabilization. *Int J Numer Methods Eng* 69:1671–1716
2. Bischoff M, Ramm E (1997) Shear deformable shell elements for large strains and rotations. *Int J Numer Methods Eng* 40:4427–4449
3. de Sousa RJA, Cardoso RPR, Valente RAF, Yoon JW, Gracio JJ, Jorge RMN (2005) A new one-point quadrature enhanced assumed strain (EAS) solid-shell element with multiple integration points along thickness: part I—geometrically linear applications. *Int J Numer Methods Eng* 62:952–977
4. de Sousa RJA, Cardoso RPR, Valente RAF, Yoon JW, Gracio JJ, Jorge RMN (2006) A new one-point quadrature enhanced assumed strain (EAS) solid-shell element with multiple integration points along thickness—part II: nonlinear applications. *Int J Numer Methods Eng* 67:160–188
5. Vu-Quoc L, Tan XG (2003) Optimal solid shells for non-linear analyses of multilayer composites. I. Statics. *Comput Methods Appl Mech Eng* 192:975–1016
6. Vu-Quoc L, Tan XG (2003) Optimal solid shells for non-linear analyses of multilayer composites. II. Dynamics. *Comput Methods Appl Mech Eng* 192:1017–1059
7. Betsch P, Gruttmann F, Stein E (1996) A 4-node finite shell element for the implementation of general hyperelastic 3D-elasticity at finite strains. *Comput Methods Appl Mech Eng* 130:57–79
8. Hauptmann R, Schweizerhof K (1998) A systematic development of 'solid-shell' element formulations for linear and non-linear analyses employing only displacement degrees of freedom. *Int J Numer Methods Eng* 42:49–69
9. Miehe C (1998) A theoretical and computational model for isotropic elastoplastic stress analysis in shells at large strains. *Comput Methods Appl Mech Eng* 155:193–233
10. Schwarze M, Reese S (2009) A reduced integration solid-shell finite element based on the EAS and the ANS concept—geometrically linear problems. *Int J Numer Methods Eng* 80:1322–1355
11. Schwarze M, Reese S (2011) A reduced integration solid-shell finite element based on the EAS and the ANS concept—large deformation problems. *Int J Numer Methods Eng* 85:289–329
12. Cardoso RPR, Jeong WY, Mahardika M, Choudry S, de Sousa RJA, Valente RAF (2007) Enhanced assumed strain (EAS) and assumed natural strain (ANS) methods for one-point quadrature solid-shell elements. *Int J Numer Methods Eng* 75:156–187
13. Freischläger C, Schweizerhof K (1996) On a systematic development of trilinear three-dimensional solid elements based on Simo's enhanced strain formulation. *Int J Numer Methods Eng* 33:2993–3017
14. Doll S, Schweizerhof K, Hauptmann R, Freischläger C (2000) On volumetric locking of low-order solid and solid-shell elements for finite elastoviscoplastic deformations and selective reduced integration. *Eng Comput* 1:77–88
15. Harnau M, Schweizerhof K (2002) About linear and quadratic "solid-shell" elements at large deformations. *Comput Struct* 80:805–817
16. Klinkel S, Gruttmann F, Wagner W (1999) A continuum based three-dimensional shell element for laminated structures. *Comput Struct* 71:43–62
17. Klinkel S, Gruttmann F, Wagner W (2006) A robust non-linear solid shell element based on a mixed variational formulation. *Comput Methods Appl Mech Eng* 195:179–201
18. Simo JC, Rifai MS (1990) A Class of mixed assumed strain methods and the method of incompatible modes. *Int J Numer Methods Eng* 29:1595–1638
19. Andelfinger U, Ramm E (1993) EAS-elements for 2D, 3D, plate and shell structures and their equivalence to HR-elements. *Int J Numer Methods Eng* 36:1311–1337
20. Klinkel S, Wagner W (1997) A geometrical non-linear brick element based on the EAS-method. *Int J Numer Methods Eng* 40:4529–4545
21. Fraeijns de Veubeke BM (1951) Diffusion des inconnues hyperstatiques dans les voilures à longeron couples. *Bull. Serv. Technique de L'Aéronautique*. Imprimerie Marcel Hayez: Bruxelles 24:56
22. Hu HC (1955) On some variational principles in the theory of elasticity and plasticity. *Sci Sin Beijing* 4:33–54
23. Washizu K (1955) On some variational principles in the theory of elasticity and plasticity. *Aeroelastic and Structures Research Laboratory, Massachusetts Institute of Technology*. Technical Report 25-18
24. Simo JC, Armero F (1992) Geometrically nonlinear enhanced-strain mixed methods and the method of incompatible modes. *Int J Numer Methods Eng* 33:1413–1449
25. Bathe KJ (1996) *Finite element procedures*. Prentice Hall, Englewood Cliffs
26. Hughes TJR, Tezduyar TE (1981) Finite elements based upon Mindlin plate theory with particular reference to the four-node isoparametric element. *J Appl Mech* 48:587–596
27. Dvorkin EN, Bathe KJ (1984) Continuum mechanics based four-node shell element for general non-linear analysis. *Eng Comput* 1:77–88
28. Militello C, Felippa CA (1990) A variational justification of the assumed natural strain formulation of finite elements—I. Variational principles. *Comput Struct* 34:431–438
29. Militello C, Felippa CA (1990) A variational justification of the assumed natural strain formulation of finite elements—II. The C^0 four-node plate element. *Comput Struct* 34:439–444
30. Betsch P, Stein E (1995) An assumed strain approach avoiding artificial thickness straining for a nonlinear 4-node shell element. *Commun Numer Methods Eng* 11:899–909
31. de Sousa RJA, Jorge RMN, Valente RAF, Sa JMAC (2003) A new volumetric and shear locking-free 3D enhanced strain element. *Eng Comput* 20:896–925
32. de MacNeal RH, Harder RL (1985) A proposed standard set of problems to test finite element accuracy. *Finite Elements Anal Des* 1:3–20
33. Morley LSD (1963) *Skew plates and structures*. Pergamon Press, Oxford
34. Scordelis AC, Lo KS (1969) Computer analysis of cylindrical shells. *J Am Concr Inst* 61:539–561
35. Belytschko T, Leviathan I (1994) Physical stabilization of the 4-node shell element with one point quadrature. *Comput Methods Appl Mech Eng* 113:321–350
36. Stanley GM (1985) *Continuum-based shell elements*. PhD thesis, Stanford University Stanford, Stanford
37. Parisch H (1995) A continuum-based shell theory for nonlinear applications. *Int J Numer Methods Eng* 38:1855–1883
38. Valente RAF, de Sousa RJA, Jorge RMN (2004) An enhanced strain 3D element for large deformation elastoplastic problems in thin-shell applications. *Comp Mech* 34:38–52
39. Valente RAF, Jorge RMN, Cardoso RPR, de Sa JMAC, Grácio JJA (2003) On the use of an enhanced transverse shear strain shell element for problems involving large rotations. *Comput Mech* 30:286–296

40. Brank B, Peric D, Damjanic FB (1995) On implementation of a nonlinear four node shell finite element for thin multilayered elastic shells. *Comput Mech* 16:341–359
41. Whitney JM (1969) Bending-extensional coupling in laminated plates under transverse load. *J Compos Mater* 3:20–28
42. Spilker RL, Jakobs DM (1986) Hybrid stress reduced-Mindlin elements for thin multilayer plates. *Int J Numer Methods Eng* 23:555–578